Published in: *ACS Nano* **13**, 4402–4409 (2019)
https://doi.org/10.1021/acsnano.8b09645

Photo-Driven Dipole Reordering: Key to Carrier Separation in Metalorganic Halide Perovskites

Hung-Chang Hsu[1], Bo-Chao Huang[2], Shu-Cheng Chin[1], Cheng-Rong Hsing[2], Duc-Long Nguyen[2, 6, 7], Michael Schnedler[3], Raman Sankar[4, 8], Rafal E. Dunin-Borkowski[3], Ching-Ming Wei[2, 6], Chun-Wei Chen[5, 9, 10], Philipp Ebert[3], and Ya-Ping Chiu[1, 9]

[1]*Department of Physics, National Taiwan University, Taipei 10617, Taiwan*

[2]*Institute of Atomic and Molecular Sciences, Academia Sinica, Taipei 10617, Taiwan*

[3] *Peter Grünberg Institut, Forschungszentrum Jülich GmbH, 52425 Jülich, Germany*

[4] *Institute of Physics, Academia Sinica, Taipei 11529, Taiwan*

[5] *Department of Materials Science and Engineering, National Taiwan University, Taipei 10617, Taiwan*

[6] *Molecular Science and Technology Program, TIGP, Academia Sinica, Taipei 10617, Taiwan*

[7] *Department of Physics, National Central University, Taoyuan City 32001, Taiwan*

[8]*Center for Condensed Matter Sciences, National Taiwan University, Taipei 10617, Taiwan*

[9] *Center of Atomic Initiative for New Materials, National Taiwan University, Taipei 10617, Taiwan*

[10] *Taiwan Consortium of Emergent Crystalline Materials (TCECM), Ministry of Science and Technology, Taipei 10617, Taiwan*

Abstract：

Photo-driven dipole reordering of the intercalated organic molecules in halide perovskites has been suggested to be a critical degree of freedom, potentially affecting physical properties, device performance, and stability of hybrid perovskite–based optoelectronic devices. However, thus far a direct atomically-resolved dipole mapping under device operation condition, i.e. illumination, is lacking. Here, we map simultaneously the molecule dipole orientation pattern and the electrostatic potential with atomic resolution using photo-excited cross-sectional scanning tunneling microscopy and spectroscopy. Our experimental observations demonstrate that a photo-driven molecule dipole reordering, initiated by a photo-excited separation of electron-hole pairs in spatially displaced orbitals, leads to a fundamental reshaping of the potential landscape in halide perovskites, creating separate one-dimensional transport channels for holes and electrons. We anticipate that analogous light-induced polarization order transitions occur in bulk and are at the origin of the extraordinary efficiencies of organometal halide perovskite-based solar cells as well as could reconcile apparently contradictory materials' properties.

Introduction

In the search for the most economical yet still highly efficient solar cell material, halide perovskites developed rapidly toward the materials of choice due to their rather inexpensive production costs on almost any substrate, combined with remarkable power conversion efficiencies reaching over 20%.[1-4] The success of halide perovskites has been suggested to stem from their surprising materials' properties, i.e. large carrier lifetimes and long diffusion lengths,[5-9] leading to low carrier recombination rates, as well as high absorption.[10] The elucidation of the physical origins of these notable properties and conversion efficiencies led to an exceptionally intense research activity and the suggestion of different competing physical mechanisms. For example, theoretical calculations predict that the relative orientations of the intercalated $CH_3NH_3^+$ (methylammonium, MA) organic molecule cations are critical for understanding the carrier conduction. Since these organic cations exhibit a polarization, their orientation is expected to induce local potential fluctuations and lead to random ferroelectric domains walls.[11-13] Interestingly, *ordered* ferroelectric domain walls are predicted to induce potential fluctuations, separating the localization of holes and electrons,[12-14] thereby reducing carrier recombination.[13, 15] Other calculations suggest in contrast that the tilting/distortion of the octahedrons induces a localization of carriers[12] and changes of the band gap.[16-17] Although several previous works emphasize the important role of organic cation dipole's orientation on the charge carrier separation, the only *indirect* experimental result stems from neutron scattering and suggests that the rotation of the MA organic molecule cation affects the electrical conductance.[18]

Furthermore, understanding organometal halide perovskites in actual operating devices requires investigations under illumination.[19-22] Such studies are highly critical in view of the remarkable recent observation of a light-induced giant dielectric constant[23-25] and prediction of switching of (macroscopic) ferroelectric domains.[26-27] These effects may be related to a light-induced reordering of the MA organic molecule cations and thermalization of carriers[26, 28], but thus far there is no direct *real-space* microscopic experimental proof of any of these theories. Previous microscopic approaches by scanning tunneling microscopy lack a mapping of the potential landscape and, more importantly, provide no atomically resolved investigation under *simultaneous* illumination.[29-30]

In this work, we use cross-sectional scanning tunneling microscopy (XSTM) and spectroscopy (XSTS) to study fundamental illumination-induced physical effects in methylammonium lead bromide perovskites ($CH_3NH_3PbBr_3$ also referred to as $MAPbBr_3$) single crystals, cleaved in ultrahigh vacuum, under simultaneous light illumination with atomic resolution. We perform an atomically resolved mapping of the spatial orientation of the intercalated $CH_3NH_3^+$ organic cations and the electrostatic

potential at (001) cleavage surfaces in the as-cleaved state in dark and under laser illumination. We find an additional degree of freedom, a photo-driven order transition of the organic cation dipole orientation pattern transforms a polarization structure with overlapping electron and hole transport paths in dark conditions into a new one under illumination with one-dimensional atomic-scale potential wells, creating separate conduction channels for electrons and holes. The underlying mechanism is a photo-excited separation of electron-hole pairs in spatially displaced orbitals, creating a polarization field, which initiates a reordering of the intercalated polarized organic molecule cation. Analogous *illumination-induced* polarization order transitions in the bulk can be anticipated to be at the origin of the remarkable efficiency and carrier conduction properties of organometal halide perovskites and their solar cells.

Results

Based on the bulk structure of orthorhombic $CH_3NH_3PbBr_3$, cleaved (001) surfaces can be terminated either by Pb-Br or by $CH_3NH_3^+$- Br^- (MA-Br) layers (**Fig. 1A**). In the corresponding constant-current STM images shown in **Fig. 1B** and **1C**, respectively, the bright protrusions reveal the positions of the Br surface atoms.[17, 29, 31-32] The Pb-Br surface termination does not contain MA organic cations (see **Fig. 1A**) and exhibits a 2×2-like rectangular pattern, resulting from the orthorhombic crystal structure. For the mapping of the dipole orientations of the intercalated MA organic molecule cations, the highest possible sensitivity is achieved at the surface termination with a MA-Br top layer. **Fig. 1C** illustrates a typical cleavage surface with a MA-Br top layer, revealing two types of surface reconstructions labeled dimer and zigzag structure, highlighted in yellow and green, respectively. [29-30] The dominant dimer structure exhibits alternatingly increased and reduced Br-Br separation along <110> directions, leading to dimers (**Fig. 1D**). In contrast, the zigzag structure forms zigzag rows of Br atoms along the [100] direction (**Fig. 1E**). The different surface reconstructions arise from different dipole orientation patterns of the intercalated MA ($CH_3NH_3^+$) organic molecule cations.[29] The Coulomb interaction between the negatively charged Br^- and the dipole of the polarized $CH_3NH_3^+$ organic cation induces an attraction or repulsion depending on the orientation of the MA organic molecule cations. Hence, the displacements of the Br^- are the signatures of the orientation of the dipoles of the neighboring organic molecule cations, not visible themselves in the STM images. [29] **Figs. 1D** and **E** show the dimer and zigzag structure with the dipole of the MA organic cations indicated by white arrows, respectively. For example, in **Fig. 1D**, the two Br atoms nearby the positive side of the organic cations' dipole are shifted toward the organic cation, whereas those facing the negative side of the dipole are repelled, creating a 2×2 periodicity as indicated by the dotted unit cell.

In order to understand the effect of the dipole orientation of organic cations on the transport of free charge carriers, the local electrostatic potential landscape is deduced. The methodology is presented in the following first. A quantity directly related to the surface electrostatic potential ϕ is the work function Φ of $CH_3NH_3PbBr_3$, through $e \cdot \Delta\phi = \Delta\Phi$. The spatial fluctuations of the work function of $CH_3NH_3PbBr_3$, $\Delta\Phi$, can be extracted from the exponential decay of the tunnel current (I) with tip-sample separation (Δz), given by [33-35]

$$I \propto \exp(-2\kappa \times \Delta z), \quad (1)$$

with κ being the inverse decay constant

$$\kappa = \frac{\sqrt{2mB}}{\hbar}. \quad (2)$$

The energy barrier B experienced by the tunneling electrons with mass m is approximated by $B = (\Phi_{\mathrm{Tip}} + \Phi)/2$, with Φ_{Tip} being the work function of the tungsten tip. **Figs. 2** illustrates such measurements: First, $I(\Delta z)$ curves measured on the dimer structure at the center position of a dimer (blue circle in **Fig. 2A**) and in between of dimers (red circle) are shown in **Fig. 2E**. The solid lines illustrate a fit of Eq. (1) to the data revealing an exponential decay. The obtained κ is mapped two-dimensionally in **Figs. 2B** and **2D** for surface areas with dimer and zigzag structure, respectively.

The κ maps reveal characteristic spatial variations corresponding according to Eq.(2) to fluctuations of the potential energy. **Fig. 2F** shows the κ values (left axis) measured at four equivalent positions in between of two Br^- atoms with different surrounding organic cation dipole alignments, as indicated by the respective arrows. The right axis shows the corresponding $\Delta\Phi$. For the dimer structure, the head-to-head and the tail-to-tail dipole alignments yield a κ of ~0.86 and ~0.81 $Å^{-1}$, respectively, corresponding to an electrostatic potential energy difference of 0.68 eV. In contrast, in the zigzag structure with ferroelectric dipole alignments the potential energy difference in between of the Br^- atoms is much smaller, i.e. ~ 0.12 eV, consistent with theory. [36]

The derivation of the MA organic molecule cation dipole orientation pattern is corroborated by **Fig. 3A-C** using the example of the dominating 2×2 dimer surface structure observed in dark. The calculated STM image (**Fig. 3B**) based on the dipole pattern shown schematically in **Fig. 3C** agrees excellently with the measured STM image (**Fig. 3A**), corroborating Ref. 29.

Thus far, we only investigated the dipole orientation pattern in dark, without illumination. However, under laser illumination a fundamentally different new dominant 4×2 surface structure forms reversibly, characterized by a ×4 modulation along the [1-10] direction and a ×2 modulation along the perpendicular [110] direction (**Fig. 3D**). The reversibility towards the 2×2 dimer structure in dark, shown in the supporting information (**Fig. S1**), demonstrates the presence at all times of the organic

cations. Hence, a photo-driven reordering of the dipole orientations of the MA organic cations takes place.

Therefore, we derive a map of the surface organic cation dipole orientation by analyzing the displacements of the Br atoms observed at the surface along the three symmetry lines labeled A-A′, B-B′, and C-C′ in **Fig. 3D**:

(i) The overall square like structure and the observation of bright (high LDOS) and dark (low LDOS) stripes along the [110] direction indicates that the dipoles must be oriented primarily perpendicular to the surface plane, but in the opposite direction, i.e. the negative side up in the bright stripes (B-B′) and the positive side up in the dark stripes (C-C′).

(ii) The ×2 periodicity along the [110] direction indicates that the dipoles in the center of the bright (B-B′) and dark (C-C′) stripes are *in addition* inclined along the [110] direction, resulting a modulation of the degree of polarization and hence of the repulsive (attractive) forces exerted on the Br atoms in the bright (dark) stripes. This leads to the dipole orientation patterns along B-B′ and C-C′ illustrated schematically in **Fig. 3F**.

(iii) Finally, taking into account the opposite perpendicular dipole orientation between the bright and dark stripes (see (i) above), the dipole of the organic cation in between has to be primarily in-plane oriented. Since the overall Br atoms exhibit an almost perfect square lattice, the in plane dipoles of the organic cation are likely alternatingly pointing toward B-B′ and C-C′ lines. The resulting dipole orientation pattern along the A-A′ line consists of consecutive 90° rotated organic cations as schematically illustrated in the structural model in **Fig. 3F**. The good agreement of the simulated (**Fig. 3E**) and experimental STM images (**Fig. 3D**) confirms the derived illumination-induced organic cation molecule dipole orientation pattern.

The dipole orientation pattern under illumination is overall antiferroelectric. However, along the B-B′ and C-C′ lines the dipole orientations are always pointing down and upward, respectively, creating local ferroelectricity. This is corroborated by the nanoscale domain pattern observed in **Fig. 4**. Two types of 4×2 domains occur alternatingly (labeled A and B domain), which are shifted against each other by half a unit cell along the ×4 periodicity. This leads to a nanoscale pseudoperiodic reversal of the out-of-plane organic molecule dipole orientations along the [110] direction, e.g. along the B-B′ line. This formation of an antiferroelectrically ordered nanoscale domain pattern compensates the local ferroelectricity of the illumination induced 4×2 structure and corroborates the derived molecule orientation pattern.

The illumination also changes drastically the potential energy landscape. **Figs. 5A and D** show the spatial variation of the inverse decay constant κ extracted from $I(\Delta z)$ curves measured at every pixel position without and with light illumination,

respectively. A comparison of both inverse decay constant maps points to a very spotty distribution in dark, transforming to a one-dimensional pattern under illumination. In order to extract the potential energy landscapes $e \cdot \Delta\phi$, local corrugation effects[37] were removed by averaging the inverse decay constants within a unit cell. The resulting potential energy landscapes without and with illumination are shown in **Figs. 5B** and **E**, respectively. We also simulated the theoretical potential maps of the dimer phase in the dark (**Fig. 5C**) and the 4×2 structure under illumination (**Fig. 5F**). Both simulated potential maps agree well with the experimentally observed ones.

In dark, the electrostatic potential energy landscape exhibits a weak checkerboard-like pattern over the entire cleaved surface with local minima and maxima (see **Fig. 5B**). In contrast, under illumination (**Fig. 5E**), the electrostatic potential energy landscape is dominated by a strong one-dimensional valley and hill pattern aligned along the [1-10] direction with significantly larger modulation as compared to the case without illumination.

Discussion

This drastic modification of the potential energy landscape affects carrier transport: In the dark, the potential energy fluctuations are too weak to create spatially separate conduction channels for electrons and holes. In terms of transport paths, the spotty pattern of the potential energy fluctuations and the lack orientational confinement create many crossing points of hole and electron pathways, as graphically suggested by the large fading out of the pathways (**Fig. 6A**). Hence, the probability of recombination increases. However, under illumination the reordering of the organic cation dipoles creates deep one-dimensional potential energy wells with an average depth of ~150 meV. The one-dimensional potential wells can be rationalized on basis of the relative orientation of neighboring organic cation dipoles. Along the atomic rows in [1-10] direction neighboring dipoles always exhibit a perpendicular arrangement (A-A' in **Fig. 3F**). As shown in **Fig. 2F** this 90° rotated arrangement leads to very small potential fluctuations. In contrast, in [110] direction, the organic cation dipoles have a head to head or tail to tail component (see model along B-B' and C-C' in **Fig. 3F**), which was found to create a large potential energy modulation (**Fig. 2F**). Hence, the light-induced organic cation dipole orientation pattern creates strong one-dimensional potential energy wells, avoiding crossing points of hole and electron pathways (**Fig. 6B**), effectively increasing the carrier lifetime.

We found an atomic-scale dipole reordering upon illumination inducing fundamental transformations of the potential landscape at organometal halide perovskite cleavage *surfaces*. In order to check if the *bulk* material undergoes an illumination induced reordering too, we performed macroscopic resistance

measurements of the same crystal. They yield a pronounced one-dimensional reduction in resistance upon illumination (supporting information 2), anticipating that illumination of organometal halide perovskites will induce reordering of the intercalated organic molecule dipoles in the bulk, too.

Finally, we turn to the physical mechanisms driving the photo-induced dipole reordering. The electromagnetic field of the incident light itself cannot account for the reordering, since a sub-bandgap illumination with same intensity does not induce any reordering. Similarly, following Fouriers' heat conduction law, the used laser irradiance induces only negligible heating (<2 K) for our sample dimensions and the materials' thermal conductivity of 0.4-0.5 $Wm^{-1}K^{-1}$.[38-39] Only when electron-hole pairs are photo generated, a reordering takes place. This points to an electronically-induced dipole reorientation via excited charge carriers, which can be explained as follows: Illumination induces a weakening of the Coulomb interaction between the halide atom and the MA molecule cations by photo excitation of an electron from the hybridized Pb 6s–halide 5p orbital (at valence band maximum) into the Pb 6p orbital at the conduction band edge, as suggested by Ref. 20. This leads to a spatial separation of the electron and hole pair, due to the transfer of the electron from close to the halide atom site to the Pb site within the unit cell, creating a polarization field. One can anticipate that the intercalated polarized MA molecule cation rotates in this photo-induced polarization field to counteract it. It can be expected that the rotation is enabled by the prior weakening of the Coulomb interaction between the MA molecule cation and the halide atom and thus lowering of the rotation barrier by electron-hole pair generation. Hence, this suggests that the photo-induced reordering of the MA molecule orientation pattern is a counteraction to a photo-induced polarization arising from excitation in spatially shifted orbital states within a unit cell.

Conclusions

We discovered a photo-induced atomic-scale reordering of the intercalated MA molecule cations at organometal halide perovskite surfaces using cross-sectional scanning tunneling microscopy. The rotation of the polarized MA molecule cations is suggested to be initiated by a photo-induced polarization created by excitation of electron-hole pairs in spatially displaced orbital states. The reordering is connected with a fundamental transformation of the potential landscape toward one-dimensional potential wells, suggesting a separation of charge carriers and hence enhancement of carrier lifetimes. Macroscopic resistance data indicate that the photo-induced reordering effect is also present in the bulk. This may in analogy lead to the creation of potential wells in the bulk, separating hole-electron pairs. The therewith expected increased carrier lifetime would provide a novel interpretation of the high photoelectric

conversion efficiencies of organometal halide perovskites. Furthermore, our results indicate that MA molecule cation dipole (re)ordering by illumination needs to be generally considered as additional degree of freedom for understanding the perovskites' characteristics and for reconciling of apparently contradictory properties. Such transitions are likely to be central for developing a comprehensive physical picture of charge carrier dynamics and high photovoltaic performance in organometal halide perovskites under actual operation conditions.

Methods:

Cross-sectional STM measurements

For our high resolution STM imaging, we cleaved $CH_3NH_3PbBr_3$ single crystals on their (001) plane in ultrahigh vacuum (~ 2×10^{-11} mbar) at 4.3 K to expose a clean and stoichiometric cross-section through the sample. $CH_3NH_3PbBr_3$ ($MAPbBr_3$) was chosen because large single crystals, with high stability in air, can be grown easily and the material exhibits a reproducibly cleavable (001) plane. Therefore, $MAPbBr_3$ is used as a model system for the investigation of the light-induced dipole reordering with atomic resolution. Furthermore, in view of technological applications it is critical to investigate the orthorhombic phase of $CH_3NH_3PbBr_3$. At room temperature, $CH_3NH_3PbBr_3$ exhibits disordered orthorhombic distortions of the unit cells, whereas below 160 K a pure orthorhombic phase forms, exhibiting larger ordered domains with cell parameters of a=7.97Å, b=8.58Å, and c=11.85Å.[40] In this work, we investigate the *pure* orthorhombic phase (T<160K) in order to unravel the fundamental molecular dipole ordering behavior in absence of grain boundaries and domain walls. This provides access to the *intrinsic* molecular dipole degree of freedom in organic-inorganic perovskites. The cleavage surfaces of the stable orthorhombic phase of $CH_3NH_3PbBr_3$ were directly investigated with atomic resolution without interruption of the vacuum while keeping the samples cooled at 4.3 K. For measurements in the dark, the cooling shield was fully closed. For constant laser illumination we used a laser diode emitting unpolarized light of a wavelength of 532 nm focused onto the sample to reach a surface irradiance of 140 mW/cm^2.

Theoretical calculations

The theoretical calculations are based on the density functional theory (DFT) [41-42] using projector augmented-wave (PAW) potentials [43], as implemented in the plane-wave-based Vienna *ab initio* simulation package [44-45]. The exchange-correlation interaction of electrons was treated using the PBE approximation functional with van der Waals corrections (vdW-D3)[46]. The surface structure was obtained by fully relaxing the top two layers (MA-Br and Pb-Br layers) while keeping the four bottom layers (two Pb-Br

and two MA-Br layers) fixed at their bulk positions (with lattice parameters a=7.97Å, b=8.58Å and c=11.85Å). The dimer structure was resulted from the (001)-2×2 surface reconstruction with MA-Br termination, and the geometry optimization is performed until the residual force was smaller than 20 meV/Å. Under laser illumination, we created a structure model based on the experimental observation by comparing the simulated STM image to the experimental measurement. For this we fixed the top layer atoms in a 4×2 surface structure, while the bottom five layers (three Pb-Br and two MA-Br layers) were fixed at their bulk positions. The vacuum region above the surface is about 20 Å wide. The plane-wave energy cutoff was set at 500 eV and the *k*-point meshes of (2×2×1) and (2×1×1) were used to sample the surface Brillouin zone for the dimer and 4×2 structures, respectively. In order to prevent an unphysical dipole interaction between two neighboring surfaces of a slab model and to obtain a correct local electrostatic potential, a dipole correction scheme[47] was applied for all DFT calculations.

Acknowledgement:
This work was financially supported by the Ministry of Science and Technology of Taiwan (Contract No. MOST 106-2628-M-002 -011 -MY3), National Taiwan University (Contract No. NTU-107L7848), and the Center of Atomic Initiative for New Materials, National Taiwan University, Taipei, Taiwan from the Featured Areas Research Center Program within the framework of the Higher Education Sprout Project by the Ministry of Education (MOE) in Taiwan. Bo-Chao Huang acknowledges financial support from Academia Sinica through the investigator award (AS-IA-107-M03) given to Prof. Yuh-Lin Wang. The authors also thank Prof. Li-Min Wang, Tien-Wei Yan, and Tiong-Jin Khou for the macroscopic resistance measurement.

Additional information:
Supplementary information 1 demonstrates the reversibility of the photo-driven dipole reordering. We find again the same initial 2×2 dimer structure when illumination was turned off, which is directly induced by the presence of an antiferroelectric dipole ordering. Supplementary information 2 shows the macroscopic resistance measurement of the $MAPbBr_3$ crystal. We find that illumination leads to a drastic reduction of the resistivity along one direction only, while along the other direction the resistivity remains unchanged. This matches the illumination-induced change of the potential landscape observed in our STM measurements.

Correspondence and requests for materials should be addressed to Y.P.C. and P.E.

References:

1. Jeon, N. J.; Noh, J. H.; Yang, W. S.; Kim, Y. C.; Ryu, S.; Seo, J.; Seok, S. I., Compositional engineering of perovskite materials for high-performance solar cells. *Nature* **2015,** *517*, 476.
2. Yang, W. S.; Noh, J. H.; Jeon, N. J.; Kim, Y. C.; Ryu, S.; Seo, J.; Seok, S. I., High-performance photovoltaic perovskite layers fabricated through intramolecular exchange. *Science* **2015,** *348* (6240), 1234-1237.
3. Wu, Y.; Yang, X.; Chen, W.; Yue, Y.; Cai, M.; Xie, F.; Bi, E.; Islam, A.; Han, L., Perovskite solar cells with 18.21% efficiency and area over 1 cm^2 fabricated by heterojunction engineering. *Nat. Energy* **2016,** *1*, 16148.
4. Luo, D.; Yang, W.; Wang, Z.; Sadhanala, A.; Hu, Q.; Su, R.; Shivanna, R.; Trindade, G. F.; Watts, J. F.; Xu, Z.; Liu, T.; Chen, K.; Ye, F.; Wu, P.; Zhao, L.; Wu, J.; Tu, Y.; Zhang, Y.; Yang, X.; Zhang, W.; Friend, R. H.; Gong, Q.; Snaith, H. J.; Zhu, R., Enhanced photovoltage for inverted planar heterojunction perovskite solar cells. *Science* **2018,** *360* (6396), 1442-1446.
5. Leng, K.; Abdelwahab, I.; Verzhbitskiy, I.; Telychko, M.; Chu, L.; Fu, W.; Chi, X.; Guo, N.; Chen, Z.; Chen, Z.; Zhang, C.; Xu, Q.-H.; Lu, J.; Chhowalla, M.; Eda, G.; Loh, K. P., Molecularly thin two-dimensional hybrid perovskites with tunable optoelectronic properties due to reversible surface relaxation. *Nat. Mater.* **2018,** *17*, 908–914.
6. Saidaminov, M. I.; Abdelhady, A. L.; Murali, B.; Alarousu, E.; Burlakov, V. M.; Peng, W.; Dursun, I.; Wang, L.; He, Y.; Maculan, G.; Goriely, A.; Wu, T.; Mohammed, O. F.; Bakr, O. M., High-quality bulk hybrid perovskite single crystals within minutes by inverse temperature crystallization. *Nat. Commun.* **2015,** *6*, 7586.
7. Xing, G.; Mathews, N.; Sun, S.; Lim, S. S.; Lam, Y. M.; Grätzel, M.; Mhaisalkar, S.; Sum, T. C., Long-Range Balanced Electron- and Hole-Transport Lengths in Organic-Inorganic $CH_3NH_3PbI_3$. *Science* **2013,** *342* (6156), 344-347.
8. Elbaz, G. A.; Straus, D. B.; Semonin, O. E.; Hull, T. D.; Paley, D. W.; Kim, P.; Owen, J. S.; Kagan, C. R.; Roy, X., Unbalanced Hole and Electron Diffusion in Lead Bromide Perovskites. *Nano Lett.* **2017,** *17* (3), 1727-1732.
9. Wei, H.; Fang, Y.; Mulligan, P.; Chuirazzi, W.; Fang, H.-H.; Wang, C.; Ecker, B. R.; Gao, Y.; Loi, M. A.; Cao, L.; Huang, J., Sensitive X-ray detectors made of methylammonium lead tribromide perovskite single crystals. *Nat. Photon.* **2016,** *10*, 333.
10. Chen, Z.; Dong, Q.; Liu, Y.; Bao, C.; Fang, Y.; Lin, Y.; Tang, S.; Wang, Q.; Xiao, X.; Bai, Y.; Deng, Y.; Huang, J., Thin single crystal perovskite solar cells to harvest below-bandgap light absorption. *Nat. Commun.* **2017,** *8* (1), 1890.
11. Frost, J. M.; Butler, K. T.; Walsh, A., Molecular ferroelectric contributions to anomalous hysteresis in hybrid perovskite solar cells. *APL Mater.* **2014,** *2* (8), 081506.

12. Liu, S.; Zheng, F.; Koocher, N. Z.; Takenaka, H.; Wang, F.; Rappe, A. M., Ferroelectric Domain Wall Induced Band Gap Reduction and Charge Separation in Organometal Halide Perovskites. *J. Phys. Chem. Lett.* **2015,** *6* (4), 693-699.
13. Frost, J. M.; Butler, K. T.; Brivio, F.; Hendon, C. H.; van Schilfgaarde, M.; Walsh, A., Atomistic Origins of High-Performance in Hybrid Halide Perovskite Solar Cells. *Nano Lett.* **2014,** *14* (5), 2584-2590.
14. Bi, F.; Markov, S.; Wang, R.; Kwok, Y.; Zhou, W.; Liu, L.; Zheng, X.; Chen, G.; Yam, C., Enhanced Photovoltaic Properties Induced by Ferroelectric Domain Structures in Organometallic Halide Perovskites. *J. Phys. Chem. Lett. C* **2017,** *121* (21), 11151-11158.
15. Pecchia, A.; Gentilini, D.; Rossi, D.; Auf der Maur, M.; Di Carlo, A., Role of Ferroelectric Nanodomains in the Transport Properties of Perovskite Solar Cells. *Nano Lett.* **2016,** *16* (2), 988-992.
16. Motta, C.; El-Mellouhi, F.; Kais, S.; Tabet, N.; Alharbi, F.; Sanvito, S., Revealing the role of organic cations in hybrid halide perovskite $CH_3NH_3PbI_3$. *Nat. Commun.* **2015,** *6*, 7026.
17. Zhang, Z.; Long, R.; Tokina, M. V.; Prezhdo, O. V., Interplay between Localized and Free Charge Carriers Can Explain Hot Fluorescence in the $CH_3NH_3PbBr_3$ Perovskite: Time-Domain Ab Initio Analysis. *J. Am. Chem. Soc.* **2017,** *139* (48), 17327-17333.
18. Leguy, A. M. A.; Frost, J. M.; McMahon, A. P.; Sakai, V. G.; Kockelmann, W.; Law, C.; Li, X.; Foglia, F.; Walsh, A.; O'Regan, B. C.; Nelson, J.; Cabral, J. T.; Barnes, P. R. F., The dynamics of methylammonium ions in hybrid organic–inorganic perovskite solar cells. *Nat. Commun.* **2015,** *6*, 7124.
19. Tsai, H.; Asadpour, R.; Blancon, J.-C.; Stoumpos, C. C.; Durand, O.; Strzalka, J. W.; Chen, B.; Verduzco, R.; Ajayan, P. M.; Tretiak, S.; Even, J.; Alam, M. A.; Kanatzidis, M. G.; Nie, W.; Mohite, A. D., Light-induced lattice expansion leads to high-efficiency perovskite solar cells. *Science* **2018,** *360* (6384), 67-70.
20. Zhou, Y.; You, L.; Wang, S.; Ku, Z.; Fan, H.; Schmidt, D.; Rusydi, A.; Chang, L.; Wang, L.; Ren, P.; Chen, L.; Yuan, G.; Chen, L.; Wang, J., Giant photostriction in organic–inorganic lead halide perovskites. *Nat. Commun.* **2016,** *7*, 11193.
21. Wright, A. D.; Verdi, C.; Milot, R. L.; Eperon, G. E.; Pérez-Osorio, M. A.; Snaith, H. J.; Giustino, F.; Johnston, M. B.; Herz, L. M., Electron–phonon coupling in hybrid lead halide perovskites. *Nat. Commun.* **2016,** *7*, 11755.
22. Wu, X.; Tan, L. Z.; Shen, X.; Hu, T.; Miyata, K.; Trinh, M. T.; Li, R.; Coffee, R.; Liu, S.; Egger, D. A.; Makasyuk, I.; Zheng, Q.; Fry, A.; Robinson, J. S.; Smith, M. D.; Guzelturk, B.; Karunadasa, H. I.; Wang, X.; Zhu, X.; Kronik, L.; Rappe, A. M.; Lindenberg, A. M., Light-induced picosecond rotational disordering of the inorganic

sublattice in hybrid perovskites. *Sci. Adv.* **2017,** *3* (7), e1602388.
23. Juarez-Perez, E. J.; Sanchez, R. S.; Badia, L.; Garcia-Belmonte, G.; Kang, Y. S.; Mora-Sero, I.; Bisquert, J., Photoinduced Giant Dielectric Constant in Lead Halide Perovskite Solar Cells. *J. Phys. Chem. Lett.* **2014,** *5* (13), 2390-2394.
24. Irina, A.; Sergejus, B.; Pascale, G.; Šarūnas, S.; Mehmet, S.; Gerhard, L.; Christian, F.; Jaroslavas, B.; Vytautas, S.; Maksim, I.; Brahim, D.; Juras, B.; V., S. V.; C., L. D., Dielectric Response: Answer to Many Questions in the Methylammonium Lead Halide Solar Cell Absorbers. *Adv. Energy Mater.* **2017,** *7* (19), 1700600.
25. Nie, W.; Blancon, J.-C.; Neukirch, A. J.; Appavoo, K.; Tsai, H.; Chhowalla, M.; Alam, M. A.; Sfeir, M. Y.; Katan, C.; Even, J.; Tretiak, S.; Crochet, J. J.; Gupta, G.; Mohite, A. D., Light-activated photocurrent degradation and self-healing in perovskite solar cells. *Nat. Commun.* **2016,** *7*, 11574.
26. Wu, T.; Collins, L.; Zhang, J.; Lin, P.-Y.; Ahmadi, M.; Jesse, S.; Hu, B., Photoinduced Bulk Polarization and Its Effects on Photovoltaic Actions in Perovskite Solar Cells. *ACS Nano* **2017,** *11* (11), 11542-11549.
27. Wang, P.; Zhao, J.; Wei, L.; Zhu, Q.; Xie, S.; Liu, J.; Meng, X.; Li, J., Photo-induced ferroelectric switching in perovskite $CH_3NH_3PbI_3$ films. *Nanoscale* **2017,** *9* (11), 3806-3817.
28. Park, M.; Kornienko, N.; Reyes-Lillo, S. E.; Lai, M.; Neaton, J. B.; Yang, P.; Mathies, R. A., Critical Role of Methylammonium Librational Motion in Methylammonium Lead Iodide ($CH_3NH_3PbI_3$) Perovskite Photochemistry. *Nano Lett.* **2017,** *17* (7), 4151-4157.
29. Ohmann, R.; Ono, L. K.; Kim, H.-S.; Lin, H.; Lee, M. V.; Li, Y.; Park, N.-G.; Qi, Y., Real-Space Imaging of the Atomic Structure of Organic–Inorganic Perovskite. *J. Am. Chem. Soc.* **2015,** *137* (51), 16049-16054.
30. She, L.; Liu, M.; Zhong, D., Atomic Structures of $CH_3NH_3PbI_3$ (001) Surfaces. *ACS Nano* **2016,** *10* (1), 1126-1131.
31. Wang, J.; Zhang, A.; Yan, J.; Li, D.; Chen, Y., Revealing the properties of defects formed by CH_3NH_2 molecules in organic-inorganic hybrid perovskite $MAPbBr_3$. *Appl. Phys. Lett.* **2017,** *110* (12), 123903.
32. Wang, Y.; Lü, X.; Yang, W.; Wen, T.; Yang, L.; Ren, X.; Wang, L.; Lin, Z.; Zhao, Y., Pressure-Induced Phase Transformation, Reversible Amorphization, and Anomalous Visible Light Response in Organolead Bromide Perovskite. *J. Am. Chem. Soc.* **2015,** *137* (34), 11144-11149.
33. Vitali, L.; Levita, G.; Ohmann, R.; Comisso, A.; De Vita, A.; Kern, K., Portrait of the potential barrier at metal–organic nanocontacts. *Nat. Mater.* **2010,** *9*, 320.
34. Rienks, E. D. L.; Nilius, N.; Rust, H.-P.; Freund, H.-J., Surface potential of a polar oxide film: FeO on Pt(111). *Phys. Rev. B* **2005,** *71* (24), 241404.

35. Schulz, F.; Drost, R.; Hämäläinen, S. K.; Demonchaux, T.; Seitsonen, A. P.; Liljeroth, P., Epitaxial hexagonal boron nitride on Ir(111): A work function template. *Phys. Rev. B* **2014,** *89* (23), 235429.
36. Jiang, J.; Pachter, R.; Yang, Y.; Bellaiche, L., Dependence of the Electronic and Optical Properties of Methylammonium Lead Triiodide on Ferroelectric Polarization Directions and Domains: A First Principles Computational Study. *J. Phys. Chem. Lett. C* **2017,** *121* (28), 15375-15383.
37. Landrock, S.; Jiang, Y.; Wu, K. H.; Wang, E. G.; Urban, K.; Ebert, P., Origin of nanoscale potential fluctuations in two-dimensional semiconductors. *Appl. Phys. Lett.* **2009,** *95* (7), 072107.
38. Pisoni, A.; Jaćimović, J.; Barišić, O. S.; Spina, M.; Gaál, R.; Forró, L.; Horváth, E., Ultra-Low Thermal Conductivity in Organic–Inorganic Hybrid Perovskite $CH_3NH_3PbI_3$. *J. Phys. Chem. Lett.* **2014,** *5* (14), 2488-2492.
39. Kovalsky, A.; Wang, L.; Marek, G. T.; Burda, C.; Dyck, J. S., Thermal Conductivity of $CH_3NH_3PbI_3$ and $CsPbI_3$: Measuring the Effect of the Methylammonium Ion on Phonon Scattering. *J. Phys. Chem. Lett. C* **2017,** *121* (6), 3228-3233.
40. Page, K.; Siewenie, J. E.; Quadrelli, P.; Malavasi, L., Short-Range Order of Methylammonium and Persistence of Distortion at the Local Scale in $MAPbBr_3$ Hybrid Perovskite. *Angew. Chem. Int. Ed.* **2016,** *55* (46), 14320-14324.
41. Hohenberg, P.; Kohn, W., Inhomogeneous Electron Gas. *Phys. Rev.* **1964,** *136* (3B), B864-B871.
42. Kohn, W.; Sham, L. J., Self-Consistent Equations Including Exchange and Correlation Effects. *Phys. Rev.* **1965,** *140* (4A), A1133-A1138.
43. Blöchl, P. E., Projector augmented-wave method. *Phys. Rev. B* **1994,** *50* (24), 17953-17979.
44. Kresse, G.; Furthmüller, J., Efficiency of ab-initio total energy calculations for metals and semiconductors using a plane-wave basis set. *Comp Mater. Sci.* **1996,** *6* (1), 15-50.
45. Kresse, G.; Furthmüller, J., Efficient iterative schemes for ab initio total-energy calculations using a plane-wave basis set. *Phys. Rev. B* **1996,** *54* (16), 11169-11186.
46. Grimme, S.; Antony, J.; Ehrlich, S.; Krieg, H., A consistent and accurate ab initio parametrization of density functional dispersion correction (DFT-D) for the 94 elements H-Pu. *J. Chem. Phys.* **2010,** *132* (15), 154104.
47. Neugebauer, J.; Scheffler, M., Adsorbate-substrate and adsorbate-adsorbate interactions of Na and K adlayers on Al(111). *Phys. Rev. B* **1992,** *46* (24), 16067-16080.

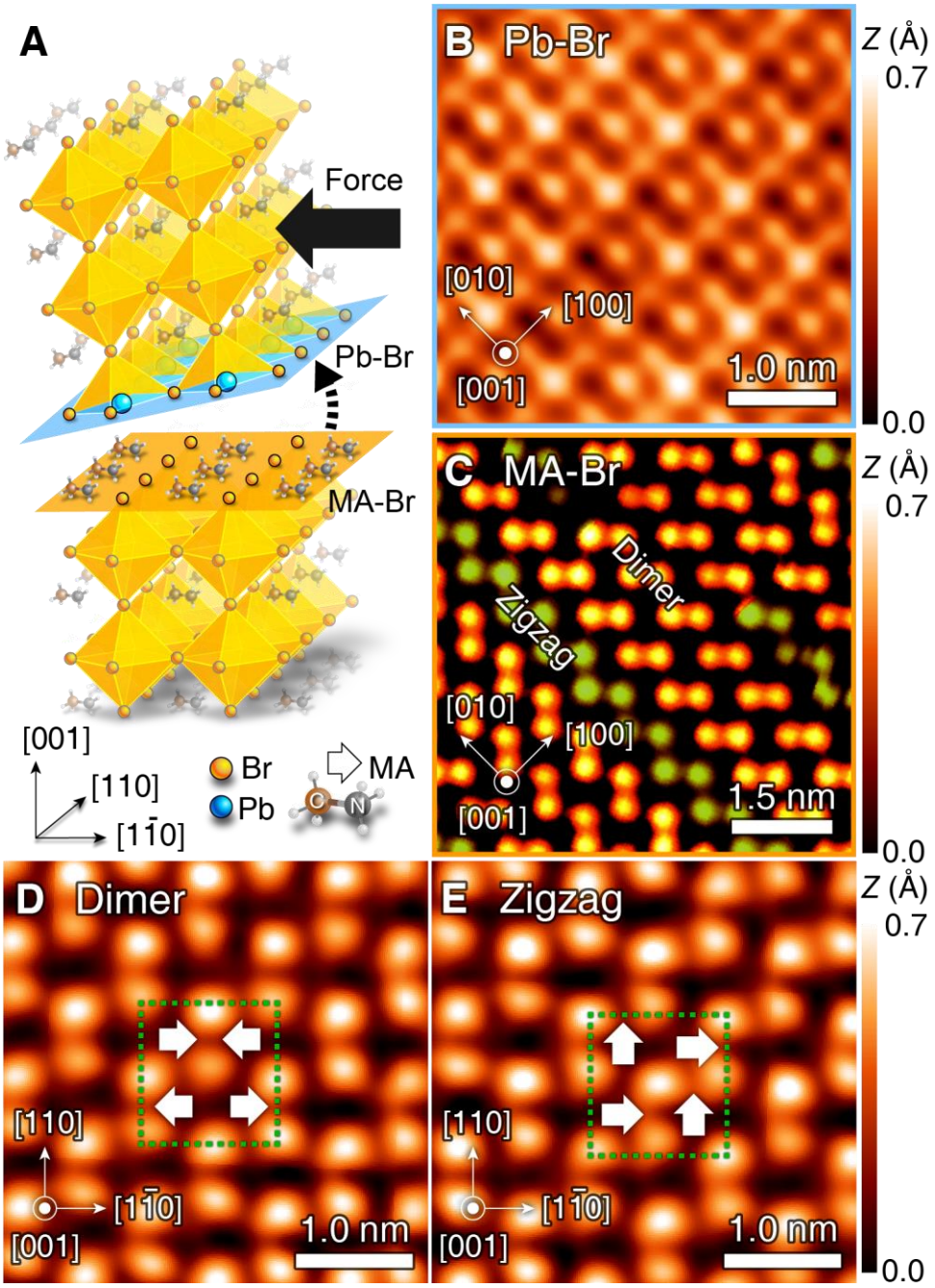

Fig. 1. (**A**) Schematic of the cleavage of $MAPbBr_3$ crystals (with orthorhombic Miller indices) leading to two types of surface terminations, i.e. with (**B**) Pb-Br and (**C**) $CH_3NH_3^+$- Br^- top layers. The polar intercalated $CH_3NH_3^+$ molecule cations are shown as brown-grey dumbbell in the structural model. The $CH_3NH_3^+$ molecules exhibit a dipole, which is denoted by a white arrow pointing from the carbon atom (C^-) to nitrogen atom (N^+). Atomically-resolved constant-current STM images of a (**B**) Pb-Br and (**C**) $CH_3NH_3^+$- Br^- terminated surface. The $CH_3NH_3^+$- Br^- terminated surface in (**C**)

consists of a dominating so called dimer structure (highlighted in a yellow color scale) and a zigzag structure (highlighted in a greenish color scale). (**D**) and (**E**) illustrate the orientation of the dipole of the $CH_3NH_3^+$ molecule (white array) between the Br atoms leading to the dimer and zigzag structures, respectively. The STM images were acquired at -5.5 V and 200 pA. The dotted rectangle marks the unit cell in (**D**) and (**E**).

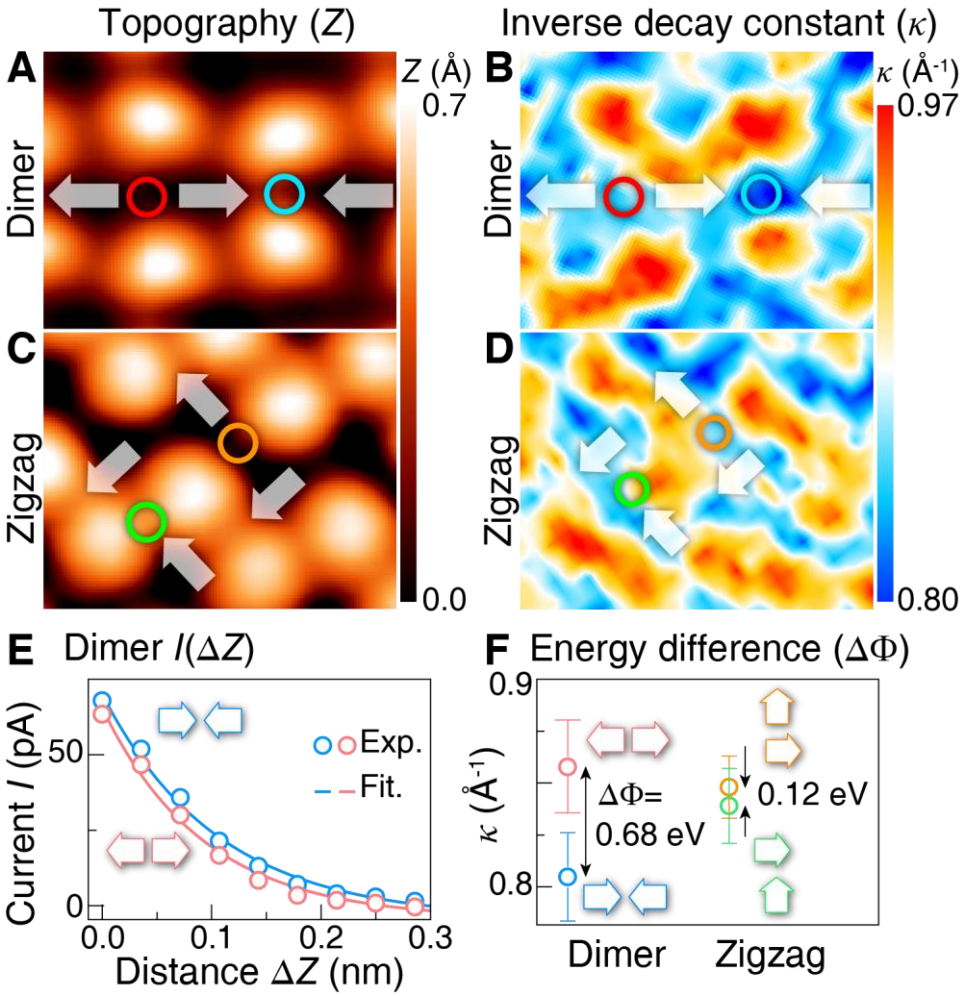

Fig. 2. High resolution STM images of (**A**) the dimer and (**C**) the zigzag structures, with corresponding inverse decay constant (κ) map shown in (**B**) and (**D**), respectively. (**E**) The tunneling current (*I*) as the function of the tip-sample distance (Δ*z*) for the head-to-head (blue circle) and the tail-to-tail (red circle) $CH_3NH_3^+$ molecule dipole alignments in (**A**). (**F**) κ values and corresponding work function or electrostatic potential energy differences ($e\cdot\triangle\phi$) for different $CH_3NH_3^+$ molecule dipole alignments in dimer and zigzag domain structures marked by colored circles in (**A**) and (**C**).

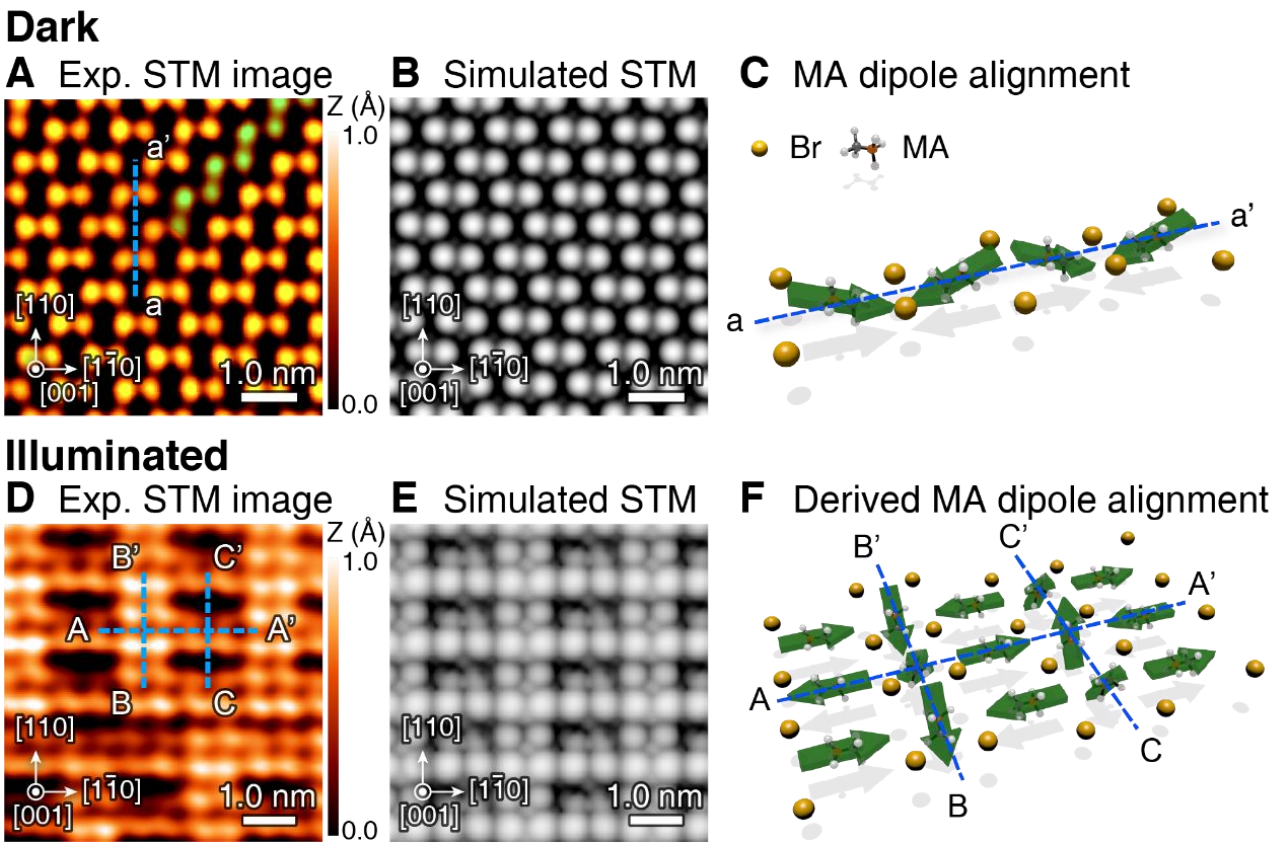

1 **Fig. 3.** Comparison of the surface structure and molecule orientation pattern (**A**-**C**) in
2 the dark and (**D**-**F**) under illumination. The STM images reveal a transition from (**A**)
3 the dominant dimer structure in the dark to (**D**) a 4×2 structure under laser illumination.
4 The simulated STM image (**B**) in the dark and (**E**) under laser illumination are derived
5 from the $CH_3NH_3^+$ molecule dipole alignments shown schematically in (**C**) and (**F**)
6 under dark and illuminated conditions, respectively.

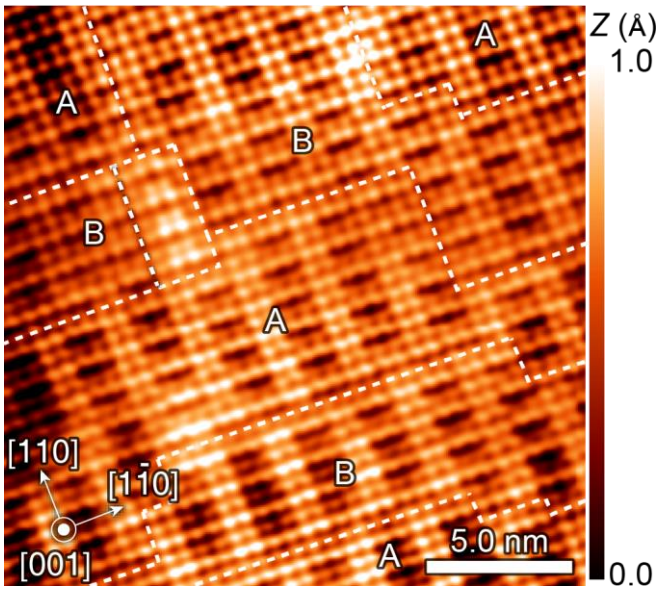

Fig. 4. The formation of an antiferroelectrically ordered nanoscale domain pattern under illumination.

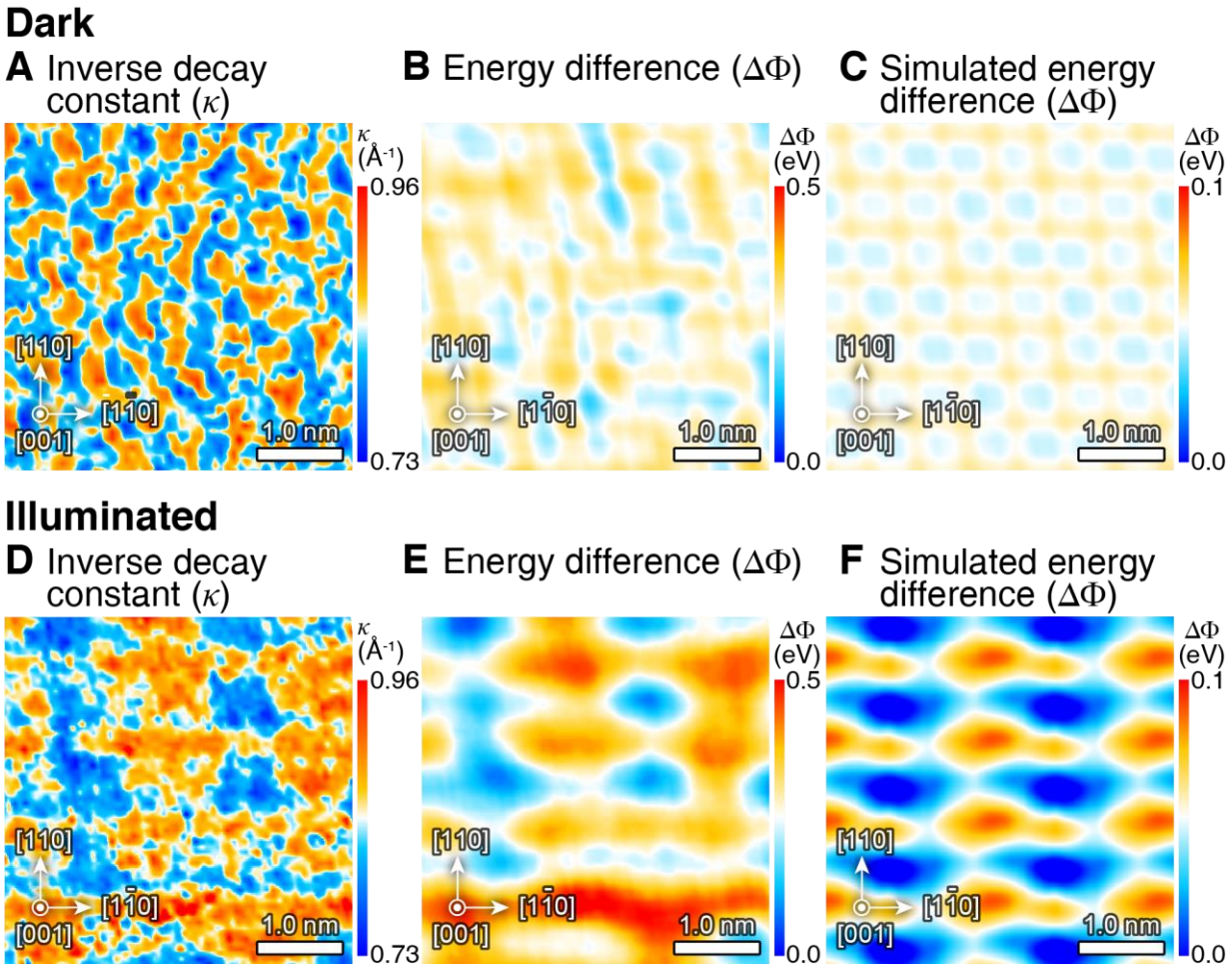

Fig. 5. Comparison of the spatial variation of the inverse decay constant κ and the therefrom derived electrostatic potential energy (**A**, **B**) in dark and (**D**, **E**) under illumination. The electrostatic potential energy landscapes in (**B**, **E**) are extracted from the respective κ maps (**A**, **D**) as described in the text, removing local density of states effect due to the corrugation of Br atoms by averaging over a surface unit cell area. (**C**, **F**) Theoretically calculated two-dimensional maps of the potential energy difference (**C**) in dark and (**F**) under light illumination based on the 2×2 and 4×2 structural models illustrated in Fig. 3**C** and 3**F**, respectively.

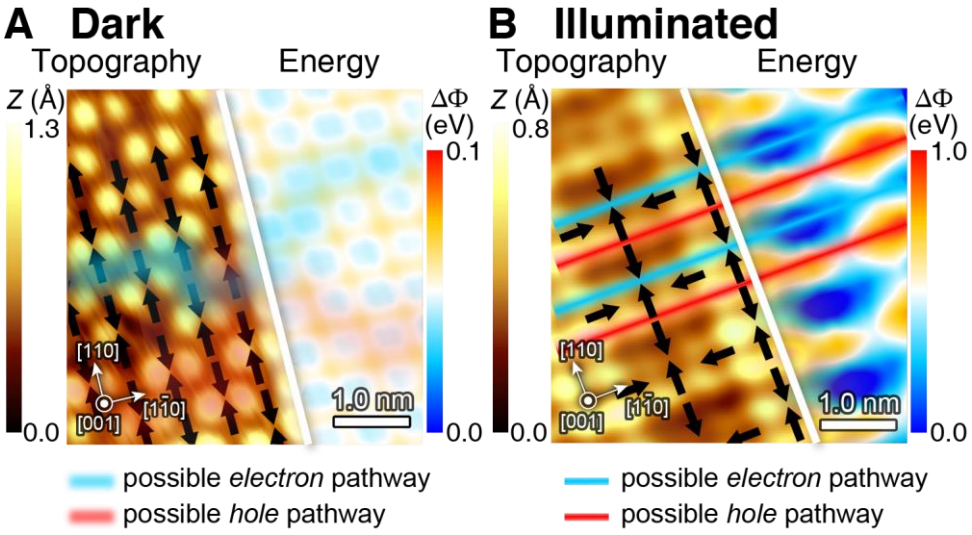

Fig. 6. The schematic illustration of possible charge carrier pathways in (**A**) the 2×2 phase in dark and (**B**) the illumination-induced 4×2 phase superimposed on the constant current STM images (left side) and electrostatic potential energy landscapes (right). The orientation of $CH_3NH_3^+$ molecule dipoles are indicated by arrows as defined in **Fig. 1A**. The blue lines indicate a low electron potential energy pathway and the red ones indicate a low hole potential energy pathway. The fading out illustrates the lack of potential modulation in the 2×2 phase in dark.